Chiral Gold Nanowires with Boerdijk−Coxeter−Bernal Structure

Yihan Zhu,*[†] Jiating He,[‡] Cheng Shang,[§] Xiaohe Miao,[||] Jianfeng Huang,[†] Zhipan Liu,[§] Hongyu Chen,*[‡] and Yu Han*[†]

[†]Advanced Membranes and Porous Materials Center, Physical Sciences and Engineering Division and [||]Catalysis Research Center, King Abdullah University of Science and Technology, Thuwal 23955-6900, Saudi Arabia

[‡]Division of Chemistry and Biological Chemistry, Nanyang Technological University, Singapore 637371

[§]Shanghai Key Laboratory of Molecular Catalysis and Innovative Materials, Department of Chemistry, Fudan University, Shanghai 200433, China

S *Supporting Information*

ABSTRACT: A Boerdijk−Coxeter−Bernal (BCB) helix is made of linearly stacked regular tetrahedra (*tetrahelix*). As such, it is chiral without nontrivial translational or rotational symmetries. We demonstrate here an example of the chiral BCB structure made of totally symmetrical gold atoms, created in nanowires by direct chemical synthesis. Detailed study by high-resolution electron microscopy illustrates their elegant chiral structure and the unique one-dimensional "pseudo-periodicity". The BCB-type atomic packing mode is proposed to be a result of the competition and compromise between the lattice and surface energy.
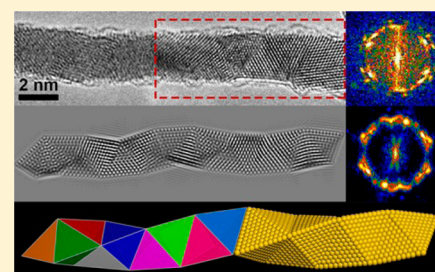
INTRODUCTION

The assembly of chiral crystals from highly symmetric atoms, i.e., the origin of chirality,[1] is of fundamental importance. In practice, one can approach this difficult problem by exploring new structures and studying their formation mechanism.[2] As the collective properties of atoms are highly dependent on their packing modes, unusual atomic packing, such as those of quasicrystals,[3] is of great significance. In applications, chiral crystals, particularly metallic ones, have a great promise for introducing enantioselectivity in chemical separation,[4] sensing,[5] and catalysis.[4a,6]

Bulk chiral crystals have a long history,[7] but chiral nanostructures are only an emerging field. Organic and metallic chiral nanowires (NWs) have been reported.[1b] While chirality can be inherited from the packing of chiral organic molecules, the origin of chirality in metallic NWs is intriguing. Few modes are known for the chiral self-assembly of totally symmetric spheres (atoms).

To date, there are only a few cases of chiral metallic nanocrystals in the literature, all in the form of NWs.[1b] This is in contrast to the large number of achiral metallic NWs reported, as dictated by the intrinsic lattice symmetry of atomic packing modes.[8] Kondo et al. prepared ultrathin Au NWs (*d* = 0.6−1.3 nm, without ligands but suspended between Au domains) by top-down etching in ultrahigh vacuum. The resulting chiral NWs contained strained helical atomic rows (nondensely packed) coiling around the wire axis.[1b] The José-Yacamán group synthesized Au−Ag alloy NWs (Au:Ag = 1:3) containing icosahedral moieties, which can be approximately described as two interwoven BCB helices (hereafter referred to as the double-strand BCB).[9] Longer Au−Ag alloy NWs with a different composition (Au:Ag = 1:1) were found to have a

similar double-strand BCB structure, whereby the unique atomic packing was responsible for causing the NWs to twist into double helices upon coating of a metal layer.[10]

Here, we report ultrathin Au NWs with an atomic packing mode that is different from all known literature examples. They are the close representation of the BCB *tetrahelix* in atomic packing, where the Au atoms are densely packed, forming a straight but overall chiral structure. The chiral atomic structure and morphology are characterized in detail. Combining *in situ* electron microscopy with theoretical simulations, we show that the surface ligands play a key role in stabilizing the unusual Au NWs. Such a structure demonstrates the feasibility of chirality in densely packed nonalloy NWs and represents an excellent example where the interplay of fundamental interactions leads to exotic structures at the nanoscale.

RESULTS AND DISCUSSION

Mathematic Model and Atomic Structure of BCB Au NWs. As a mathematic model of 1D chiral structure, *tetrahelix* is constructed by linear stacking of regular tetrahedra (Figure 1c). It becomes an atomic packing mode when the tetrahedral units are made of densely packed atoms. *Tetrahelix* was first studied by Boerdijk in 1952 using congruent spheres as the building units,[11] and it was later named as Boerdijk−Coxeter helix,[12] Bernal spiral,[13] and recently BCB helix.[14] Depending on the stacking orientation, *tetrahelix* appears as either a left-handed spiral or a right-handed one. A tetrahedron in a BCB helix rotates about a screw axis by an angle of $\cos^{-1} 2/3 \approx 131.81°$ with respect to its face-sharing neighbor. Hence, the
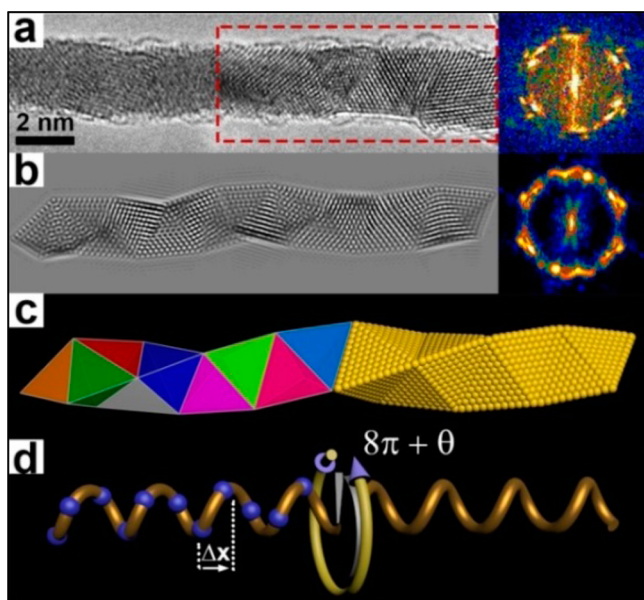
Figure 1. (a) Experimental and (b) simulated HRTEM image of a single BCB-structured Au NW ($\Delta f = -35$ nm). The corresponding FFTs are shown in the right. (c) Topological (left) and atomic (right) models of a BCB *tetrahelix*. (d) Schematic illustration of the pseudoperiodicity in BCB *tetrahelix*, where the blue dots represent the mass centers of the tetrahedral units, illustrating the relationship between their location and orientation, where Δx is the advance of each tetrahedron along the screw axis with respect to its neighbor; θ refers to the orientation difference between the twelfth tetrahedron and the first; $8\pi + \theta$ is the total rotation angle of 11 successive tetrahedra that constitute an approximate pitch.

number of tetrahedra per turn is a nonquadratic irrational number (2.7312...).[15] It means that a BCB helix is aperiodic, though a periodic approximant of BCB helix can be extracted from the polytope {3,3,5}.[15d] Previously, the construction of BCB *tetrahelix* by self-assembly has only been achieved using micrometer-sized Janus particles,[16] where the particles spiral around the wire axis and every four neighboring particles constitute a tetrahedral unit.

In a recent report, we synthesized thin ($d = 6$ nm) Au NWs using a seed-mediated substrate growth method (the active surface growth).[17] A strong ligand 4-mercaptobenzoic acid (4-MBA) inhibits Au deposition on the seeds except the "active" interface between the seed and the substrate, thus allowing the sustained unidirectional growth of the Au NWs. These NWs were typically polycrystalline with random lattice orientation. To our great interest, a radical change of structure occurred when we pushed for the thinnest NWs. Experimentally, this was achieved by using higher concentration of ligand and slower reduction rate of the Au species. We found that 3 nm was the lowest limit for the diameter of the Au NWs. When this size was reached, the Au NWs became chiral with the BCB-type structure.

As revealed by scanning electron microscopy (SEM), ultrathin Au NWs (~3 nm wide and several microns long) were successfully obtained with a high yield on the surface of the wafer (SI, Figure S1a). High-resolution transmission electron microscopy (HRTEM) was employed to investigate the structure of the Au NWs. The Si wafer was sonicated in an aqueous solution, so that the Au NWs were detached and dispersed. After centrifugation, the enriched Au NWs were dried onto the holey carbon TEM grids. Suspended in the holes

of the carbon film, most NWs studied in this work were not supported by a substrate (SI, Figure S1b). Under electron beam irradiation, these NWs easily broke and fused, with much less stability than thicker NWs.[17,18] To minimize such interference, we used a relatively low dosage of electron beam and tried to take images as quickly as possible.

Figure 1a shows an HRTEM image that indicates a possible BCB *tetrahelix* structure. Successive edge-sharing triangular domains with lattice fringes are observed at the right part of the image (the highlighted area), which resemble the projection of stacked tetrahedra with gradually twisted orientations. For easy comparison, we constructed an *in silico* model of BCB *tetrahelix* by stacking {111} faceted Au tetrahedra with an edge length (L) of 3.2 nm. That is, each tetrahedron is composed of 12 layers of Au atoms with a face-centered cubic (fcc) arrangement. HRTEM images were then simulated at different orientations under various defocusing conditions. When the model helix was oriented as illustrated in Figure 1c and a defocus value of -35 nm was applied, the simulated image showed lattice fringes closely resembling the observed ones (Figure 1b). The similarity is confirmed by comparing their corresponding fast Fourier transforms (FFTs, insets of Figure 1a,b). This result suggests that the BCB *tetrahelix* is a proper structure model for the Au NW. The left section of the NW in Figure 1a was out of focus, likely because the ultrathin NW was slightly bent.

As a consequence of the seeded growth in the active surface growth mode, the two ends of the NW are not identical. One end connecting to the seed is sometimes curved; it can be easily identified from the thicker diameter of the seed particle ($d \approx 6$ nm). The end contacting the substrate is straight with the same diameter as that of the NW body (SI, Figure S2). But the intrinsic crystal structure of this end cannot be easily determined, because the structural changes always start from the ends and broken points (vide infra).

"Pseudo-Periodicity" of BCB Au NWs. As discussed above and illustrated in Figure 1d, the orientations of the tetrahedral units vary discretely along the *tetrahelix* without any strict periodicity. In TEM experiments, however, the appearance of "similar" segments along the NW suggests 1D "periodicity". That is, a small degree of orientation deviation in terms of the tetrahedra therein does exist, but it can be tolerated in giving the "similar" TEM appearance. An example is shown in Figure 2b, where three intermittent dark (diffraction) contrast regions can be assigned as "similar", though the lattice fringes within these regions are not exactly parallel to each other upon careful inspection. This observation is consistent with the aperiodic nature of BCB *tetrahelix*.

To define a helical pitch, it is of importance to know how much orientation deviation can be tolerated, which obviously is a function of the imaging conditions but not easily predictable. In a BCB *tetrahelix*, each tetrahedron has a $(1/\sqrt{10})L$ advance and a 131.81° rotation with respect to the adjacent tetrahedron along the screw axis.[15a,c] Thus, 3 successive tetrahedra do not constitute a turn because the redundant angle ($\theta = 3 \times 131.81°$ $- 2\pi = 35.43°$) would be too large to give a recognizable repeating pattern. It would take 11 tetrahedra ($\tau_1 = (11/\sqrt{10})$ L) to constitute one approximate helical pitch, but there is still a sizable redundant angle of 9.9° ($\theta = 11 \times 131.81° - 8\pi$) between the twelfth tetrahedron and the first. In the next pitch, due to the accumulated redundant angle (θ), similar TEM patterns should appear after 8 tetrahedral units, i.e., after $(8/\sqrt{10})L$ (τ_2), where θ is $-15.63°$. That is, the aperiodic nature
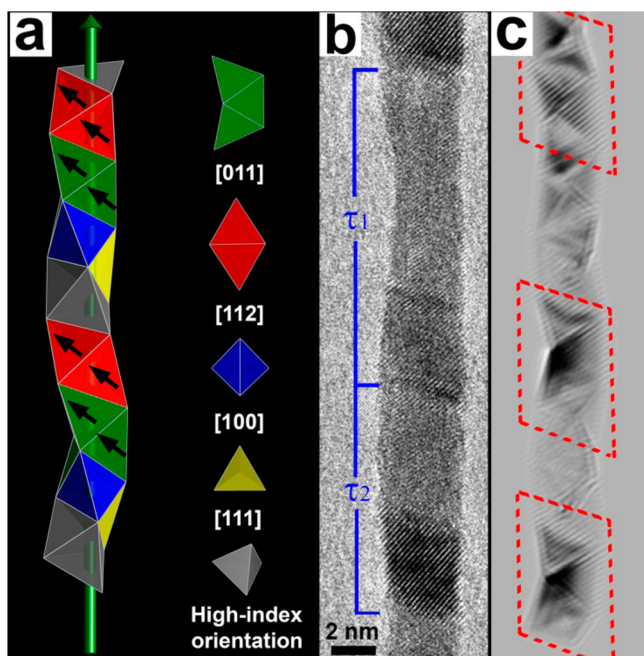
Figure 2. (a) Schematics illustrating a BCB *tetrahelix*, where the segments with different orientations are marked in different colors. Black arrows indicate the normals of the (111) planes on the $[011]$ and $[112]$ oriented trimer and dimer, respectively. (b) Experimental and (c) simulated HRTEM image of a BCB-structured Au NW with intermittent dark contrast, showing two types of helical pitches (τ_1 and τ_2). Simulation conditions: $\Delta f = -30$ nm; to simulate the vibration effect, a convolution of the image with an elliptical Gaussian of the standard deviations of 6 and 12 pm (in the 11 o'clock and 2 o'clock direction, respectively) was applied. The vibration effect in (c) causes the asymmetric damping of high-frequency information (low-frequency dark contrast becomes more apparent), and thus the simulated image appears different from Figure 1b.

of BCB *tetrahelix* should result in uneven pitch lengths distributed along the wire axis.

We systematically studied the dependence of pitch length on the level of tolerance by going through 5000 units of tetrahedra

(SI, Figure S3). If only small redundant angles ($<5°$) can be tolerated, typical pitches would contain 30, 41, or 71 tetrahedra. With larger tolerance (between $12.8°$ and $17.6°$), the pitches become shorter (8-, 11-, and 19-unit ones). The arrangement sequence of different pitches was found to depend on the orientation of the first tetrahedron (SI, Figure S4). In experiments, 19-unit pitches were too long to be observed due to the inevitable structural imperfections (e.g., bending or defects) of the real NWs. Our survey of over a dozen NWs found no pitch lengths other than τ_1 and τ_2 (8- and 11-unit pitches), indicating that the tolerance of redundant angle is probably quite large under the imaging conditions. The large tolerance was further validated through analyzing the diffraction contrast of the ultrathin Au NW (SI, Figures S5 and S6).

The observed dark contrast in Figure 2b originates from the stronger diffraction of the tetrahedral domains that are oriented close to specific low-index directions. Assuming that the incidence of the electron beam is close to the $[112]$ axis of two successive tetrahedra (a dimer, in red color), the following three successive tetrahedra (a trimer, in green color) will have their common $[011]$ zone axis nearly parallel to the beam direction (Figure 2a). The other neighboring tetrahedron (in blue color) is closely aligned with the $[100]$ axis. Given that the strongest (111) and (002) reflections appear in these directions, part of the region of these six successive tetrahedra would show darker contrast in the TEM image. The following few tetrahedra are lighter in contrast because they have orientations close to the $[111]$ or other high-index directions (Figure 2a). Similar dark contrast regions are observed along the NW with intervals of τ_1 and τ_2 (Figure 2b), which is consistent with the above analysis on helical pitches. We were able to qualitatively reproduce such intermittent dark contrasts by dynamical TEM simulation using the BCB structural model (Figure 2c). The lattice fringes observed within these dark regions were also correctly simulated, which are from the (111) reflections of the different tetrahedral units. Consistent with the TEM image, the simulated fringes are approximately parallel to each other but not exactly so. These low-frequency fringes along with the dark diffraction contrast are markedly enhanced in Figure 2b as compared with the case of Figure 1a, possibly
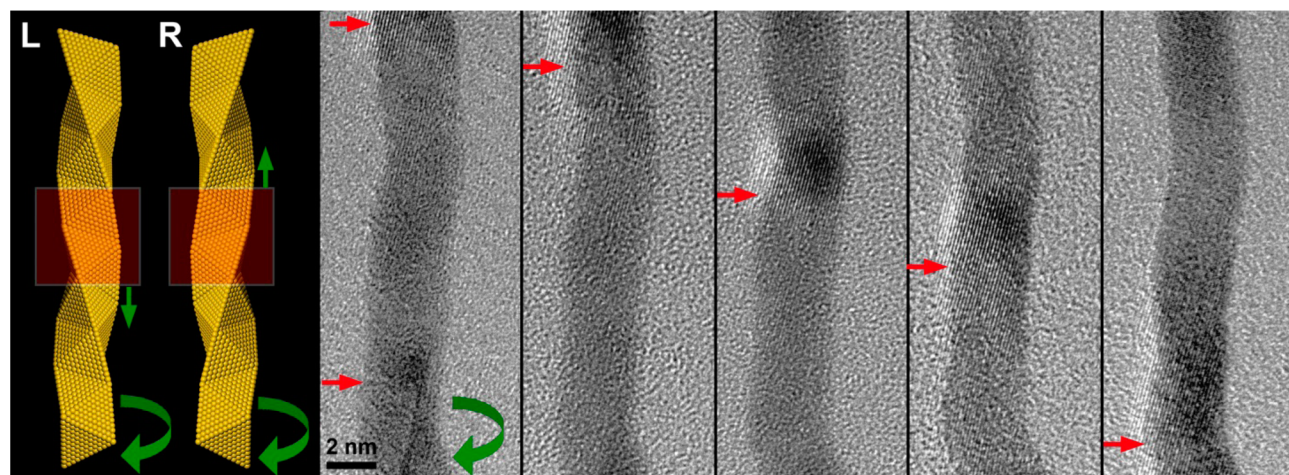

Figure 3. (left) Schematics illustrating the determination of left- and right-handedness in BCB *tetrahelices* by tilting the NWs around their screw axes. When being tilted clockwise (viewing from the top end, as indicated by the green curved arrows), the diffraction contrast arising from the highlighted region would move downward for a left-handed NW but upward for a right-handed one, as illustrated by green arrows. (right) Typical TEM images from a clockwise tilt series (~15° tilting angle per frame) of a left-handed Au NW, in which the downward movement of the dark contrast region during the specimen tilting was indicated by the red arrows.

due to the anisotropic specimen vibration, as verified by simulation (Figure 2c). This result provides strong evidence that large tolerance of orientation deviation is possible and confirms that the Au NW is a close representation of the BCB tetrahelix.

The above arguments are based on the HRTEM images, which are static 2D projections. The 3D helical nature of the Au NW can be better characterized by HRTEM upon sequential tilting of the sample. As dictated by the screw axis symmetry, with clockwise tilting around the screw axis (as defined by viewing from the top end, Figure 3), any recognizable pattern should move downward for a left-handed Au NW but upward for a right-handed one.

The AuNWs suspended in the holes of the holey carbon film were not stable enough for the tilting experiments. We had to select AuNWs sitting on top of the carbon film, which are typically more stable but gave less sharp contrast. We examined several Au NWs and found both left- and right-handed ones in the sample. Typical TEM images from a tilt series are shown in Figure 3. Upon clockwise tilting (the green arrow), the dark contrast and lattice fringe moved downward, indicating that the Au NW is left-handed. Most importantly, such movement upon specimen tilting confirmed the helical nature of the NW, supporting the BCB structural model. A suspension of the BCB Au NWs did not show chiral signals in the circular dichroism spectrum, likely because the sample was a racemic mixture consisting of equal amounts of left- and right-handed NWs. In addition, although the majority of the NWs that we observed appeared to have certain BCB characteristics, we were unable to determine the accurate percentage of chiral NWs due to the limited sampling ability of HRTEM.

Stability and Formation Mechanism of BCB Au NWs. The establishment of the BCB structure entails a series of questions regarding to its mechanism of formation. What are the principles underlying the selection between the BCB *tetrahelix* and the normal fcc NWs in the literature? Is the structure energetically favorable,[17] and if so, what are the key contributing factors? In our system, thicker Au NWs (around 6 nm) were obtained with randomly oriented fcc domains,[17] whereas the 3 nm Au NWs have the orderly BCB structure. What is the origin of this size dependence?

The multiply twinned NWs are reminiscent of the multiply twinned particles (MTPs),[19] where the key energy factors have been established as follows: The total surface energy of a nanoparticle is the sum of the facet energy times the facet area:

$$\Delta G = \sum_i \gamma_i A_i \qquad (1)$$

where γ_i is the surface energy of a given facet, and A is its area.[20] While the stable {111} facets are important, they give rise to a sharp structure, which is not optimized in terms of the surface to volume (S/V) ratio.[19a,21] In addition, there are energy penalties due to the twin plane and angular gap. Basically, the angular gap arises from the incapability of space filling by the twinned domains, inducing significant elastic strains in terms of disclination and shear.[22] It is generally more energetically costly than a twin plane, because there is less "disruption" to the metallic interactions between the close packed planes across the twin boundary. Given these complex contributions, it is conceivable that the system may not be dominated by a single factor and that the structural features reflect the competition and compromise among the various factors.

Under the premise of NW-like forms, the structural stability of the different NWs can be similarly analyzed. Comparing the BCB *tetrahelix* to the normal fcc NWs,[19a,b] the former maximizes the exposure of the favorable {111} facets[23] whereas the latter has lower S/V ratio and more favorable lattice energy (no twin planes). To render the BCB *tetrahelix* thermodynamically favorable, the benefit of {111} surface should outweigh the cost of twin planes.

We note that the BCB Au NWs have relatively smooth surfaces, unlike the projection of the model BCB *tetrahelix*, which is somewhat zigzag due to the unparallel {111} facets. To investigate such a difference, we took HRTEM images along the common [011] zone axis of three adjacent tetrahedra (a trimer) in a BCB Au NW, as the zigzag feature should be most obvious at this condition. Interestingly, the trimer was found to be accompanied by two fragmentary tetrahedra, filling the shallow concave surface (Figure 4). Such a defective structure plastering the zigzag feature improves the S/V ratio of the NWs while minimizing the detrimental effects.
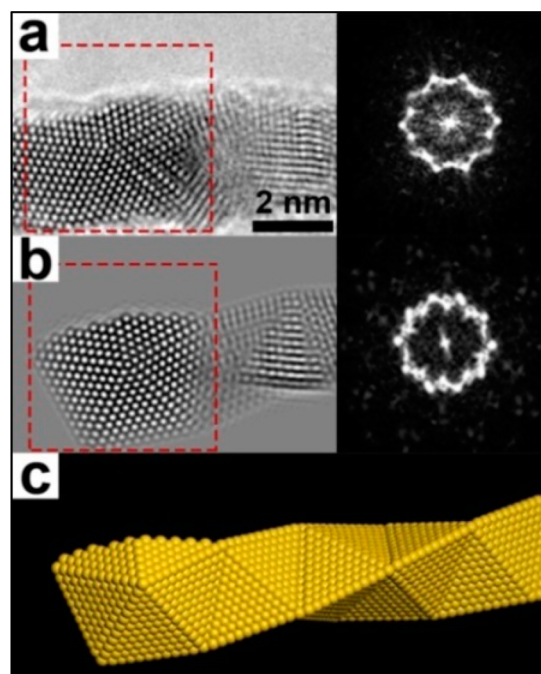

Figure 4. (a) Experimental and (b) simulated ($\Delta f = -40$ nm) HRTEM images and (c) a structural model of a BCB Au NW with fragmentary tetrahedra. The corresponding FFTs of the marked regions are shown on the right insets.

More specifically, a NW with more circular cross section should have a lower S/V ratio than one with sharp edges and corners. Though the fragmentary tetrahedra cover some of the {111} facets, the outer surface of these fragments is still optimized in terms of presenting the {111} facets among the less favorable ones. As a consequence, however, filling the concave surface creates new twin planes and angular gaps, which are similar to those in a fully developed decahedron, though much less extensive in size. It is known that the strains arising from the angular gap increases with the decahedron diameter, as more bond stretching and/or filler domains (i.e., more defects) are required to compensate for the increasing "gap" at the outer perimeter.[24] With the ultrathin fragmentary tetrahedra (<1 nm), the strain from disclinations is expected to

be easily relaxed. This argument also explains the inhibited growth of the fragmentary tetrahedra, because the strain will dramatically increase with the increase of fragment thickness.

In a sense, the underlying principle in the smoothing effects is similar to that in a truncated or rounded polyhedral nanocrystal, where the removal of sharp edges and corners improves the overall S/V ratio while preserving *most* of its stable facets. In other words, though the {111} facets in the BCB NW are not maximized to the extreme, the smoothed NW is a *best compromise* between the benefits and detriments. Hence, for the ultrathin NWs with only 3 nm diameter, the high proportion of the surface atoms leads to the dominance of the surface energy, optimizing the {111} facets at the tolerable cost of twin planes and elastic strains. The situation becomes very different when the {111} facets are not preferred or when the NW is not ultrathin (the surface energy is no longer dominating).[25] With larger area of twin planes and larger angular gaps associated with the smoothing effects, a BCB-type compromise is no longer possible. Thus, the priority would be shifted to the minimization of the twin planes and elastic strains, leading to an fcc structure.

In comparison, the double-strand BCB structure[9,10] is also optimized in terms of the {111} facets, but it contains many partial icosahedral moieties, where significant disclination strain is expected. Given the fact that both reported cases involved Au−Ag alloys, we speculate that the combination of Au−Au and Au−Ag bond distances may play a role in relaxing the strain.

Regarding the handedness of the BCB *tetrahelices*, initially both left- and right-handed NWs can form, but the subsequent growth should follow the same direction. Having both left- and right-handed sections in a same NW would produce a kink,[1b] destabilizing the NW and causing it to bend by a sharp angle.

Selection between BCB and fcc Structures. In the active surface growth, the Au nanocrystals are forced into the NW form, because the strong 4-MBA ligands induce the selective growth at the NW-substrate interface.[17] We showed that the NW growth is a dynamic competition between the Au growth at this active surface and the ligand binding at its perimeter. Thus, the NW diameter is proportional to the Au deposition rate (μ) and inversely proportional to the ligand deposition rate (γ):

$$D = \frac{4Mk}{\rho} \cdot \frac{\mu}{\gamma} = a \cdot \frac{\mu}{\gamma} \tag{2}$$

where M and ρ are the molar mass and density of Au, and D is the diameter of the NW.[17] At high ligand concentration (1.6 mM), the rapid ligand binding inhibits lateral growth at the very early stage, leading to the formation of ultrathin NWs (d = 3 nm). Thus, the BCB NWs form as they are thermodynamically favorable at such small diameters. In contrast, at low ligand concentration (0.55 mM), the formation of thick NWs (d = 6 nm) leads to the fcc NW with circular cross section (i.e., no specific facets).[17] It is also possible that the {111} facets are more favored at the higher ligand concentration.

The hypothesis is further checked for consistency with experimental observations. In particular, our experiments demonstrated the key role of ligand, whose removal reduces the stability of {111} facets, affecting the stability of the BCB Au NWs. In the TEM experiments, the ultrathin Au NWs would typically fuse upon prolonged electron beam irradiation. We found that the BCB Au NWs could survive much longer under a high voltage (300 kV) than a low one (60 kV) with

comparable dose. While this accidental discovery is counterintuitive, we note that organic matters are more vulnerable to low-voltage electron beam due to the ionization effect. Thus, the fusion of the BCB NWs is likely induced by the decomposition of the ligands, rather than the "knock-on" effect which is more pronounced at high voltage conditions. Using a high dosage of 300 kV electron beam to *gradually* remove the surface ligands, a video recording was collected showing the *in situ* transformation of a BCB NW. As shown in Figure S7 in the SI, the NW is initially nanotwinned with small domains at different orientations, indicating a BCB-type structure. With prolonged exposure to the electron beam, the NW broke into two pieces. The twinned domains in the upper section were found to gradually merge along with the disappearance of twin boundaries, giving a single-crystalline NW with the fcc structure. It is well-known that ligands have important effects on the surface energy; without them, NWs are obviously less thermodynamically stable than nanoparticles. But here, the end state still had the form of NWs, highlighting the importance of ligands in maintaining the initial BCB structure. We noted that ultrathin Au NWs (d = 3 nm) with the conventional fcc structure also broke easily in our previous experiments,[26] but their internal structure did not change during the breaking.

We performed *in situ* heating of a specimen during TEM observation to study the ligand effects on the thermal stability of the BCB NWs. The ligands capped NWs were stable up to 573 K (SI, Figure S8), showing nearly unchanged morphology. However, after the specimen was treated with O_2 plasma to remove the surface ligands, most of the NWs broke into pieces upon mild heating to 373 K, forming thick nodes or particles that have fcc structure (SI, Figure S8). These observations suggest that, without ligands to stabilize the {111} facets, the fcc structure is more favorable. Furthermore, the above-mentioned results showed that the phase transition from BCB to fcc is indeed possible.

To gain insight into the BCB-to-fcc phase transition, we simulated the collapse of a BCB helix (diameter: 8.95 Å; length: 45.41 Å; 160 atoms in total) using our recently developed stochastic surface walking (SSW) method.[27] The Gupta potential was utilized to describe the Au−Au interactions.[28] The BCB NW was set as the initial state; because it was not protected by ligands, it transformed toward an fcc NW. We ran 32 independent SSW trajectories by only allowing the elementary reactions that have barriers lower than 0.30 eV.[27] Ten out of the 32 trajectories were found to leave the BCB basin, and eight of them reached the fcc structures (see SI, Figure S9 for trajectories). As shown in Figure 5a, the BCB structure is unstable and the transition to fcc structure is highly exothermic (ΔG = 30 eV). To study the initial transition, the lowest energy reaction channel is identified from the SSW trajectories (Figure 5b, c and Movies S1−S3), in which the transition state (TS) is marked in the inset of Figure 5a. The collapse of the BCB helix starts preferentially from the end with the barrier being only 0.23 eV, giving a bulged end. In this process, the minor groove at the ending parts is first occupied by atoms diffusing from the low-coordinated ending corner. The elimination of low-coordinated corners and protruding edges causes the increase of average coordination number. The first fcc packed segment then appears while the rest part of the NW remains the helix pattern. A relatively slow wriggling process then goes on at the boundary between the fcc packed segment and the rest of BCB helix, as indicated by the smooth energy curve near the intermediate stage (IM, Figure 5a). At a
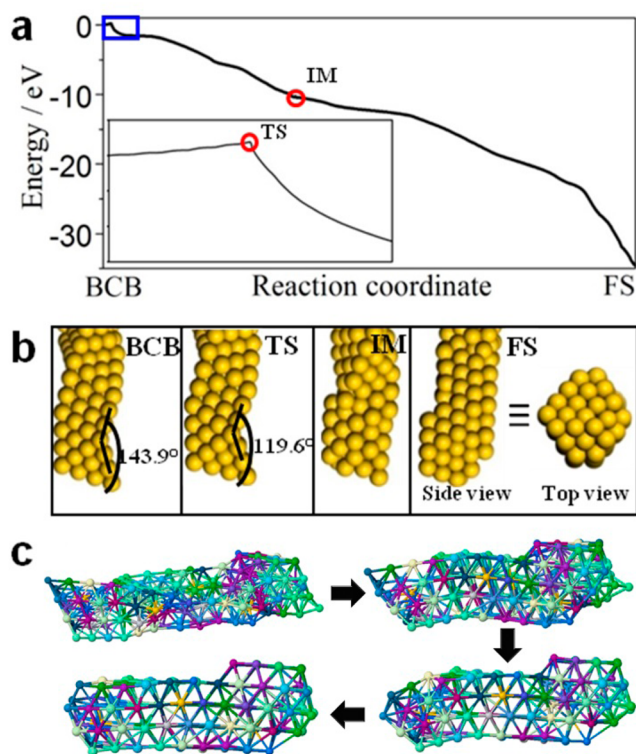
Figure 5. (a) Energy profile for the transition from a BCB *tetrahelix* to an fcc NW. The *X*-axis is the reaction coordinate along the vectors defined by the BCB ($x = 0$) and the fcc structure at the final state ($x = 1$). The transition to leave BCB (blue box) is enlarged in the inset to show the low barrier. (b) Important structures appeared along the transformation pathway, including the BCB, TS, IM, and FS, shown from two different perspectives. The average coordination numbers at the BCB, TS, and FS are 8.10, 7.89 and 8.19, respectively. (c) Key intermediates illustrating the BCB-to-fcc transformation, where the atoms are labeled in different colors for easy tracking of their motion (see Movies S1–S3 for details).

certain point, the transformation suddenly begins at the boundary and spread to the other end of the NW. Then the BCB helix finally turns into mainly three entangled fcc packed segments, as shown by the final state (FS) in Figure 5 and Movie S1.

CONCLUSIONS

We reported the synthesis and characterization of the BCB Au NWs and studied their mechanism of formation. Detailed structural information was collected with TEM, including the consecutive triangular domains, the periodicity of the repeating patterns, and the unique movement of the dark contrast upon continuous tilting of the NW. The BCB structure was consistent with these data and further supported by the TEM simulation on the basis of the model BCB *tetrahelix*. The formation of the BCB NWs was a result of the ultrathin NW diameter at the high ligand concentration. Simply put, the smoothed BCB structure is preferred because it is a best compromise between the stable {111} facets and the smoothing effects, which reduce the total surface at the cost of the twin planes and angular gaps. A holistic view is thus presented to analyze and qualitatively compare the energy contribution from all factors. Further evidence was acquired to investigate the key point of our mechanistic proposal: both the TEM experiments and the simulation of the phase transition

indicate the critical role of the surface ligands, which is consistent with the significant role played by the stable {111} facets. These understandings are critical in the exploration of chiral NWs, which are of great importance considering the combination of chirality and high surface area metallic nanostructures.

EXPERIMENTAL SECTION

Synthesis of BCB Au NWs. The ultrathin Au NWs with the BCB structure were synthesized on a Si/SiO$_2$ wafer. A Si wafer (with an area of about 0.6 cm^2) was pretreated with O$_2$ plasma for 10 min to improve its surface hydrophilicity. The pretreated Si/SiO$_2$ wafer was then reacted with the 3-aminopropyltriethoxysilane solution (5 mM) for 0.5 h to functionalize its surface with amino groups. Subsequently, the functionalized Si/SiO$_2$ wafer was soaked in the solution with excess citrate-stabilized Au seeds (3–5 nm) for 1 h to ensure the adsorption of Au seeds. The soaked Si/SiO$_2$ wafer was rinsed with water twice to remove the nonadsorbed Au seeds. The wafer was then subjected to the growth of Au NWs by immersing it in a water/ethanol (v/v = 1:1) solution containing the ligand 4-MBA (1.6 mM), HAuCl$_4$ (1.7 mM), and L-ascorbic acid (4.1 mM) for 15 min. Finally, the wafer was rinsed repeatedly with ethanol and dried in air. For detachment of the Au NWs from wafer, the nanowire-attached wafer was sonicated in water (2 mL) for 5 min. The Au NWs were then concentrated by centrifugation at 16000 *g* for 8 min to remove the supernatant. The precipitate was then dispersed by ethanol for further characterizations.

Imaging and Simulation. TEM specimen was prepared by drop-coating the ethanol suspension of Au NWs onto a holey carbon film coated Cu grid for high-resolution imaging, and an ultrathin carbon film coated Cu grid was used for the tilting experiment (Ted Pella, Inc., 300 mesh). HRTEM imaging was carried out on a FEI-Titan Super-Twin electron microscope operated at 60 or 300 kV and using a Gatan double tilt analytical holder (model 646). To ensure a high tilting angle, a Gatan high tilt tomography holder (model 916) was used in the titling experiment. *In situ* TEM experiments were carried out using a Gatan heating stage sample holder (model 652, specified to 1000 °C). HRTEM image simulation was carried out using the QSTEM code with multi-slice method (by C.T. Koch). Images with an identical pixel size of 0.04 nm/pixel were calculated based on the experimental conditions: 300 kV, *Cs* = 1.2 mm, *Cc* = 1.2 mm, convergence angle (α) of 1 mrad, energy spread (ΔE) of 0.6 eV, and total focal spread of 5 nm. The stiff Au BCB helix model used for HRTEM simulations was constructed from strain-free fcc-structured Au tetrahedral units with an edge length of 3.2 nm.

Phase-Transition Simulations. The SSW method is a method developed recently for automated exploration of potential energy surface (PES),[27] where the methodology is detailed. In brief, the SSW method follows a random direction that is refined by the biased rotation technique to drag the structural image step-wisely out of the basin region as driven by sequentially added bias Gaussian potential. A Metropolis Monte Carlo scheme is utilized to select thermodynamically more favored minimum structure. The SSW method can overcome the high barrier during the PES exploration and is therefore more efficient than the traditional molecular dynamics method for investigating the complex structural evolution.

ASSOCIATED CONTENT

Ⓢ Supporting Information

Supporting Figures S1–S9 and Movies S1–S3. This material is available free of charge via the Internet at http://pubs.acs.org.

AUTHOR INFORMATION

Corresponding Authors
yihan.zhu@kaust.edu.sa
hongyuchen@ntu.edu.sg
yu.han@kaust.edu.sa

REFERENCES

(1) (a) Pakhomov, S.; Hammer, R. P.; Mishra, B. K.; Thomas, B. N. *Proc. Natl. Acad. Sci. USA* **2003**, *100*, 3040. (b) Wang, Y.; Xu, J.; Wang, Y.; Chen, H. *Chem. Soc. Rev.* **2013**, *42*, 2930.

(2) (a) Chaikin, P. M.; Lubensky, T. C. *Principles of Condensed Matter Physics*; Cambridge University Press: Cambridge, U.K., 2000. (b) Zallen, R. *The Physics of Amorphous Solids*; Wiley: Hoboken, NJ, 1983;. (c) Bernal, J. D. In *Liquids: Structure, Properties, Solid Interactions*; Hughel, T. J., Ed.; Elsevier: Amsterdam, The Netherlands, 1965; p 25;. (d) Torquato, S. *Random Heterogeneous Materials: Microstructure and Macroscopic Properties*; Springer: New York, 2002.

(3) (a) Shechtman, D.; Blech, I.; Gratias, D.; Cahn, J. W. *Phys. Rev. Lett.* **1984**, *53*, 1951. (b) Goldman, A. I.; Widom, M. *Annu. Rev. Phys. Chem.* **1991**, *42*, 685.

(4) (a) Seo, J. S.; Whang, D.; Lee, H.; Jun, S. I.; Oh, J.; Jeon, Y. J.; Kim, K. *Nature* **2000**, *404*, 982. (b) Gabashvili, A.; Medina, D. D.; Gedanken, A.; Mastai, Y. *J. Phys. Chem. B* **2007**, *111*, 11105.

(5) Fireman-Shoresh, S.; Popov, I.; Avnir, D.; Marx, S. *J. Am. Chem. Soc.* **2005**, *127*, 2650.

(6) Johnson, B. F. G.; Raynor, S. A.; Shephard, D. S.; Mashmeyer, T.; Thomas, J. M.; Sankar, G.; Bromley, S.; Oldroyd, R.; Gladden, L.; Mantle, M. D. *Chem. Commun.* **1999**, 1167.

(7) (a) Dryzun, C.; Avnir, D. *Chem. Commun.* **2012**, *48*, 5874. (b) Flack, H. D. *Helv. Chim. Acta* **2003**, *86*, 905. (c) Imai, H.; Oaki, Y. *CrystEngComm* **2010**, *12*, 1679.

(8) (a) Cademartiri, L.; Ozin, G. A. *Adv. Mater.* **2009**, *21*, 1013. (b) Xia, Y.; Yang, P.; Sun, Y.; Wu, Y.; Mayers, B.; Gates, B.; Yin, Y.; Kim, F.; Yan, H. *Adv. Mater.* **2003**, *15*, 353. (c) Huo, Z.; Tsung, C.-k.; Huang, W.; Zhang, X.; Yang, P. *Nano Lett.* **2008**, *8*, 2041. (d) Wang, C.; Hu, Y.; Lieber, C. M.; Sun, S. *J. Am. Chem. Soc.* **2008**, *130*, 8902. (e) Lu, X.; Yavuz, M. S.; Tuan, H.-Y.; Korgel, B. A.; Xia, Y. *J. Am. Chem. Soc.* **2008**, *130*, 8900.

(9) Velázquez-Salazar, J. J.; Esparza, R.; Mejía-Rosales, S. J.; Estrada-Salas, R.; Ponce, A.; Deepak, F. L.; Castro-Guerrero, C.; José-Yacamán, M. *ACS Nano* **2011**, *5*, 6272.

(10) Wang, Y.; Wang, Q.; Sun, H.; Zhang, W.; Chen, G.; Wang, Y.; Shen, X.; Han, Y.; Lu, X.; Chen, H. *J. Am. Chem. Soc.* **2011**, *133*, 20060.

(11) Boerdijk, A. H. *Philips Res. Rep.* **1952**, *7*, 303.

(12) Coxeter, H. S. M. *Regular Complex Polytopes*; 2nd ed.; Cambridge University Press: Cambridge, U.K.1991.

(13) Bernal, J. D. *Nature* **1960**, *185*, 68.

(14) Velazquez-Salazar, J. J.; Esparza, R.; Mejia-Rosales, S. J.; Estrada-Salas, R.; Ponce, A.; Deepak, F. L.; Castro-Guerrero, C.; Jose-Yacaman, M. *ACS Nano* **2011**, *5*, 6272.

(15) (a) Lord, E. A.; Ranganathan, S. *J. Non-Cryst. Solids* **2004**, *334*, 121. (b) Sadoc, J. F.; Rivier, N. *Eur. Phys. J. B* **1999**, *12*, 309. (c) Sadoc, J. F.; Rivier, N. *Mat Sci. Eng. a-Struct* **2000**, *294*, 397. (d) Lord, E. A.; Ranganathan, S. *Eur. Phys. J. D* **2001**, *15*, 335.

(16) Chen, Q.; Whitmer, J. K.; Jiang, S.; Bae, S. C.; Luijten, E.; Granick, S. *Science* **2011**, *331*, 199.

(17) He, J.; Wang, Y.; Feng, Y.; Qi, X.; Zeng, Z.; Liu, Q.; Teo, W. S.; Gan, C. L.; Zhang, H.; Chen, H. *ACS Nano* **2013**, *7*, 2733.

(18) Guo, T.; Tan, Y. W. *Nanoscale* **2013**, *5*, 561.

(19) (a) Barnard, A. S. *Acc. Chem. Res.* **2012**, *45*, 1688. (b) Baletto, F.; Ferrando, R. *Rev. Mod. Phys.* **2005**, *77*, 371. (c) Barnard, A. S. *J. Phys. Chem. B* **2006**, *110*, 24498. (d) Howie, A.; Marks, L. D. *Philos. Mag. A* **1984**, *49*, 95.

(20) (a) Polarz, S. *Adv. Funct. Mater.* **2011**, *21*, 3214. (b) Herring, C. *Phys. Rev.* **1951**, *82*, 87.

(21) Wang, Y.; He, J.; Liu, C.; Chong, W. H.; Chen, H. *Angew. Chem., Int. Ed.* **2014**, DOI: 10.1002/anie.201402986.

(22) Johnson, C. L.; Snoeck, E.; Ezcurdia, M.; Rodriguez-Gonzalez, B.; Pastoriza-Santos, I.; Liz-Marzan, L. M.; Hytch, M. J. *Nat. Mater.* **2008**, *7*, 120.

(23) Pensa, E.; Rubert, A. A.; Benitez, G.; Carro, P.; Orive, A. G.; Creus, A. H.; Salvarezza, R. C.; Vericat, C. *J. Phys. Chem. C* **2012**, *116*, 25765.

(24) (a) Xia, Y.; Xiong, Y.; Lim, B.; Skrabalak, S. E. *Angew. Chem., Int. Ed.* **2009**, *48*, 60. (b) Martin, T. P. *Phys. Rep.* **1996**, *273*, 199.

(25) Wang, C.; Sun, S. *Chem.—Asian J.* **2009**, *4*, 1028.

(26) (a) Xu, J.; Wang, H.; Liu, C. C.; Yang, Y. M.; Chen, T.; Wang, Y. W.; Wang, F.; Liu, X. G.; Xing, B. G.; Chen, H. Y. *J. Am. Chem. Soc.* **2010**, *132*, 11920. (b) Xu, J.; Wang, Y. W.; Qi, X. Y.; Liu, C. C.; He, J. T.; Zhang, H.; Chen, H. Y. *Angew. Chem., Int. Ed.* **2013**, *52*, 6019.

(27) Shang, C.; Liu, Z. P. *J. Chem. Theory Comput.* **2013**, *9*, 1838.

(28) Cleri, F.; Rosato, V. *Phys. Rev. B* **1993**, *48*, 22.